Steady-State Analysis of Electric Springs With a Novel δ Control

Qingsong Wang, *Student Member, IEEE*, Ming Cheng, *Fellow, IEEE*, Zhe Chen, *Senior Member, IEEE*, and Zheng Wang, *Senior Member, IEEE*

***Abstract*—A novel control strategy is proposed for the recent proposed electric springs (ESs), which are connected in series with noncritical loads to form smart loads for enhancing stability of smart grid with renewable energy sources. δ control is the key concept in this paper, which is realized by controlling the phase angle of the predefined reference in a proportional resonant controller. Four critical operating functions of the ESs are analyzed with different critical loads such as resistive, inductive and capacitive types, where vector diagrams and geometric relationships are explored for δ calculation with which the ac mains voltage is regulated to the predefined value and the phase angle between the ES voltage and current is determined. With the proposed δ control, the operating modes of the ES can also be determined automatically as the input voltage varies. Operating limitations and constraints of the ESs and guidelines on how to distribute the ESs in the distributed systems are provided with δ control. Both simulation and experiment are carried out to verify the effectiveness of the proposed control strategy and theoretical analysis for the ESs.**

***Index Terms*—Distributed power systems, electric spring, operating range, phase control, renewable energy source, safety range, smart grid, stability.**

I. Introduction

ENVIRONMENTAL problem has become more and more severe all over the world. Air pollution legislations have been drafted and plans are made to raise the proportion of renewable power sources by many countries. With more and more intermittent renewable power sources such as wind energy [1], [2], the stability of power grid becomes a big issue. The key problem of instability is the mismatch between power generation and load demand. The traditional solution is to use storage devices such as batteries [3] and/or capacitors to stabilize ac mains voltage, for which reactive power compensators are typical techniques, such as the static var compensation and static synchronous compensators [4]–[7]. However, the solution relies on information and communication technology [8]–[11].

Manuscript received September 16, 2014; revised November 26, 2014; accepted January 6, 2015. Date of publication January 13, 2015; date of current version August 21, 2015. This work was supported by the National Natural Science Foundation of China under Project 51320105002 and by the Specialized Research Fund for the Doctoral Program of Higher Education of China under Project 20120092130008. Recommended for publication by Associate Editor M. Molinas.

Q. S. Wang, M. Cheng, and Z. Wang are with the School of Electrical Engineering, Southeast University, Nanjing 210096, China, and also with the Jiangsu Province Key Laboratory of Smart Grid Equipment and Technology, Nanjing 210096, China (e-mail: jeffwqs@163.com; mcheng@seu.edu.cn; zwang@seu.edu.cn).

Z. Chen is with the Department of Energy Technology, Aalborg University, Aalborg DK9220, Denmark (e-mail: zch@et.aau.dk).

Color versions of one or more of the figures in this paper are available online at http://ieeexplore.ieee.org.

Digital Object Identifier 10.1109/TPEL.2015.2391278

Based on Hooke's law for mechanical springs, the concept of electric springs (ESs) has been proposed recently as a new smart grid technology for regulating ac mains in the distributed power grid and for achieving new control paradigm of load demand following power generation [12]. Electric loads can be sorted into two categories, namely, critical loads and noncritical loads. By equipping each (or group of) noncritical loads with an ES, massive smart loads are embedded into the distributed power networks to withstand the fluctuation of ac mains to ensure stable voltage on the critical loads. The voltage regulation mechanism of the ESs is similar with mechanical springs which meet Hook's law [12].

The initial concept of the ESs for reactive power compensation has been described in [12] and the steady-state analysis and control principle with different compensation modes are presented in [13]. As a novel technology for smart grid, nevertheless, there are a lot of theoretical and technical problems need to be deeply explored. For instance, what voltage ranges that ESs can support and what the rules are for selecting parameters of key components and how to distribute the ESs in the distributed power grid. Although a circle is depicted in [12] to mention the operating limitations of the ES, specific operating ranges and safety ranges are not covered. Moreover, harmonics may be introduced based on current control strategy and need to be canceled by other methodologies [14].

In this paper, a new control strategy with a proportional resonant (PR) controller for the voltage loop and a proportional (P) controller for the current loop is proposed. By controlling the phase angle of the predefined reference of the PR controller, phase control, the so-called δ control is provided to achieve four typical compensations that the ESs can support, namely: 1) pure reactive power compensation, 2) specified power factor (PF) compensation, 3) constant real power compensation, 4) constant reactive power compensation. Vector diagrams are used to explore limitations such as effective operating ranges and safety ranges of the ESs. The proposed control and operating ranges as well have been verified by both simulation and experiments.

II. Operating Principles and Control Strategy of the ES

A. Existing Topology and Control of the ES

The application of an ES embedded in a power system is shown in Fig. 1(a), where v_G represents the renewable energy source, R_1 and L_1 are line and source impedances, Z_2 is the critical load with limited operating voltage range, Z_3 is the

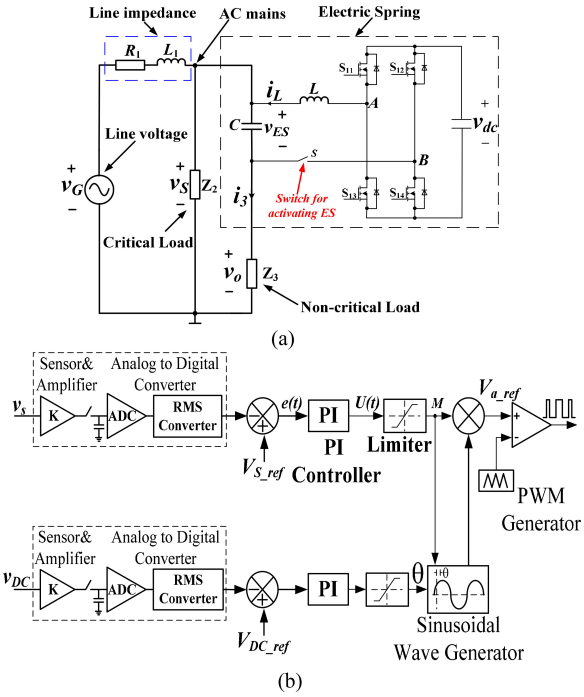

Fig. 1. Application and control of a single electric spring. (a) Application circuit of the ES. (b) Existing control of the ES.

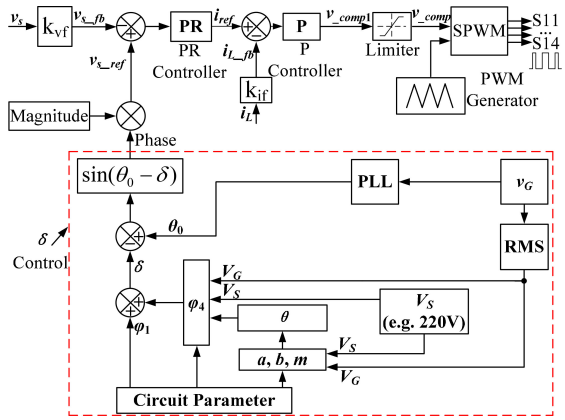

Fig. 2. Proposed control diagram of the ES.

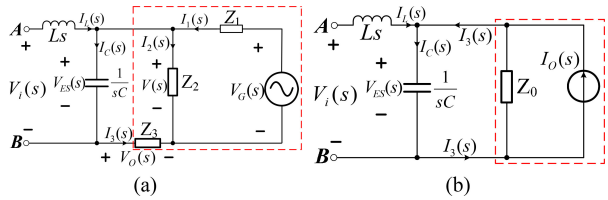

Fig. 3. Equivalent circuits of Fig. 1. (a) Equivalent circuit in s-domain. (b) Simplified circuit.

noncritical load with wide operating voltage ranges. The ES in the dashed line includes a single phase inverter and an *LC* filter. A smart load formed by an ES in series with Z_3 is in parallel with Z_2.

As described in [12]–[16], the ES is an electrical device that generates an ac voltage to regulate the voltage of critical loads while passing the fluctuating voltage (or energy) from the renewable power sources to the noncritical loads.

Classical PI controllers are used in the existing control, as shown in Fig. 1(b). Given the ES system, the control objectives of the ES are decoupled. For one objective of the critical load voltage, only an RMS block is needed and the value is compared with the predefined reference (e.g., 220 V). For another objective of pure reactive power compensation, only the RMS value of the battery voltage is sensed and the value is compared with reference value. Both objectives are simple and convenient in the application. However, harmonics may be introduced to the ES which needs additional harmonic suppression solution [14]. Besides, with double PI controllers, the relationships between different vectors may not be revealed in detail, thus the constraints would not be known. And also the effective operating range of the ES may not be found, thus the guidelines for distributing the ESs over the distributed power system could not be obtained.

B. Proposed Control Strategy of the ES

The new control diagram of the ES is proposed as shown in Fig. 2 with a PR controller used for the voltage loop in which the critical load voltage is controlled to follow a sinusoidal reference and a P controller used for current loop which controls current through inductor L. v_S is the transient voltage of the critical load, v_{s_fb} is the feedback voltage sensed from v_S multiplied by a coefficient k_{vf} (e.g., 0.1). Signal v_{s_ref} is the predefined sinusoidal reference of which the magnitude is given as needed and phase lags v_g by δ. The voltage error is used to generate reference of current loop via the PR controller. The feedback i_{L_fb} is sensed from inductor current i_L, just multiplied by a coefficient k_{if} (e.g., 0.1). The current error is used to generate the modulation signal $v_{\_\mathrm{comp}}$ via the P controller and a limiter. Four drive signals are generated by PWM generator. Obviously, the most important part in the control loop is the δ control which is phase control and directly influences reference and the control objectives.

C. System Modeling of the ES

Dynamic modeling of the ES is described in [17]. Parameter selection for the controllers can be based on circuit modeling in s-domain, shown as Fig. 3(a), which can be further simplified to Fig. 3(b), where $V_i(s)$ represents the output of the inverter and Z_0 is obtained according to the Norton's theorem

$$\begin{cases} Z_1 = R_1 + L_1 s \\ Z_2 = R_2 + L_2 s \\ Z_3 = R_3 + L_3 s \end{cases} \tag{1}$$

$$Z_0 = \frac{Z_1 Z_2 + Z_2 Z_3 + Z_3 Z_1}{Z_1 + Z_2} \tag{2}$$

$$I_0(s) = V_G(s) \times \frac{Z_2}{Z_1 Z_2 + Z_2 Z_3 + Z_3 Z_1}. \tag{3}$$

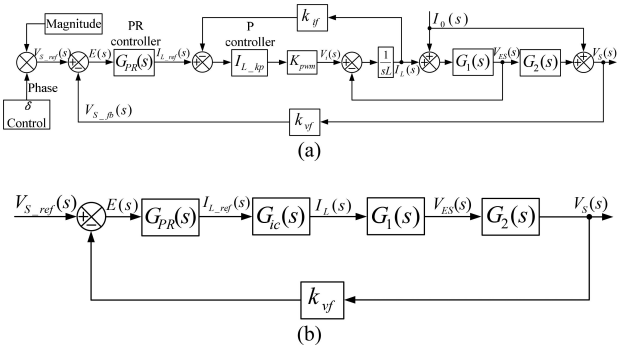

Fig. 4. Double-loop control of the ES. (a) Whole control diagram. (b) Simplified control diagram.

TABLE I
PARAMETERS OF CIRCUIT AND CONTROLLERS

Regulated mains voltage (V_S)	220 V
Battery voltage ($V_{\rm dc}$)	480 V
Line resistance (R_1)	0.1 Ω
Line inductance (L_1)	2.4 mH
Critical load (R_2)	43.5 Ω
Noncritical load (R_3)	2.2 Ω
Inductance of low-pass filter (L)	3 mH
Capacitance of low-pass filter (C)	50 μF
Feedback coefficient of voltage loop (k_{vf})	0.5
Feedback coefficient of voltage loop (k_{if})	1
V_{S_kp}	0.1
V_{S_kr}	30
I_{L_kp}	0.2

The Kirchhoff's voltage and current laws (KVL and KCL) in Fig. 3(a) are expressed as

$$sLI_L(s) = V_i(s) - V_{\rm ES}(s) \tag{4}$$

$$sCV_{\rm ES}(s) = I_L(s) + \frac{V_S(s) - V_{\rm ES}(s)}{Z_3}. \tag{5}$$

KCL in Fig. 3(b) is expressed as

$$sCV_{\rm ES}(s) = I_L(s) + I_0(s) - \frac{V_{\rm ES}(s)}{Z_0}. \tag{6}$$

Solving (6) yields

$$G_1(s) = \frac{V_{\rm ES}(s)}{I_L(s) + I_0(s)} = \frac{Z_0}{sCZ_0 + 1}. \tag{7}$$

Substituting (5) into (6) gives

$$\begin{aligned} V_S(s) &= \left(1 - \frac{Z_3}{Z_0}\right) V_{\rm ES}(s) + I_0(s) \\ &= G_2(s)V_{\rm ES}(s) + I_0(s) \end{aligned} \tag{8}$$

where

$$G_2(s) = \frac{Z_1 Z_2}{Z_1 Z_2 + Z_2 Z_3 + Z_3 Z_1}. \tag{9}$$

The critical load voltage can be solved through equations from (1) to (6), which gives

$$\begin{aligned} V_S(s) = &\frac{(Z_0 - Z_3)V_i(s)}{Z_0 LCs^2 + Ls + Z_0} \\ &+ \frac{Z_3 LCs^2 + Ls + Z_3}{Z_0 LCs^2 + Ls + Z_0} Z_0 I_0(s). \end{aligned} \tag{10}$$

Thus, the ES system can be regarded as a single phase inverter with an active load. Since $I_0(s)$ varies at a certain range, no load situation can be chosen to simplify the analysis. With PR and P controllers, the whole diagram about circuit modeling is depicted as Fig. 4(a) and simplified control diagram is shown as Fig. 4(b). $K_{\rm pwm}$ denotes the transfer function and $V_{\rm dc}$ represents the input of the single phase inverter, where $V_{\rm tri}$ is the carrier amplitude. $G_{\rm PR}(s)$ is the transfer function of the PR controller, ω_0 is 100π rad/s and ω_c is defined as $0.01\omega_0$. $K_{\rm pwm}$ and $G_{\rm PR}(s)$ are expressed as

$$K_{\rm pwm} = \frac{V_{\rm dc}}{V_{\rm tri}} \tag{11}$$

$$G_{\rm PR}(s) = V_{S\_kp} + V_{S\_kr}\frac{2\omega_c s}{s^2 + 2\omega_c s + \omega_0^2}. \tag{12}$$

The transfer function of current loop in Fig. 4(a) is defined as

$$G_{ic}(s) = \frac{I_L(s)}{I_{L\_\rm ref}(s)} = \frac{I_{L\_kp}K_{\rm pwm}}{sL + G_1(s) + k_{if}I_{L\_kp}K_{\rm pwm}}. \tag{13}$$

The closed loop transfer function in Fig. 4(b) can be expressed as

$$G_{vc}(s) = \frac{G_{\rm PR}(s)G_{ic}(s)G_1(s)G_2(s)}{1 + k_{vf}G_{\rm PR}(s)G_{ic}(s)G_1(s)G_2(s)}. \tag{14}$$

If there is no controller, the open loop transfer function from reference to output is expressed as

$$G_o(s) = K_{\rm pwm}\frac{Z_0 - Z_3}{Z_0 LCs^2 + Ls + Z_0}. \tag{15}$$

Parameter selection for controllers can be supported by system modeling above. Pole assignment is a choice in which a pair of conjugate poles are supposed to be the nearest to the vertical axis than other nondominant poles in s-domain. By comparing the coefficients of each order of the equation containing all the assumed poles with the denominator of (14), all the unknown poles together with $V_{S\_\rm kp}$, $V_{S\_\rm kr}$ and $I_{L\_\rm kp}$ will be solved. However, this method is so complicated that needs lots of mathematical formulas. A simple way is to use bode diagrams to check the parameters selected according to experience, which is adopted in this paper. An example is presented as follows and circuit parameters are list in Table I.

Final parameters are selected as list in Table I and bode diagrams of (15) and (14) are depicted in Fig. 5.

It is observed from Fig. 5(a) that almost elements at frequencies below 8805 Hz can be passed to the output if there are no controllers. In contrast, Fig. 5(b) shows that only signals within the frequency interval between 26 and 68.8 Hz are chosen to pass while all the other elements are suppressed. The method for parameter selection will be verified in the sections later. Next step is to find out the way for δ calculation.

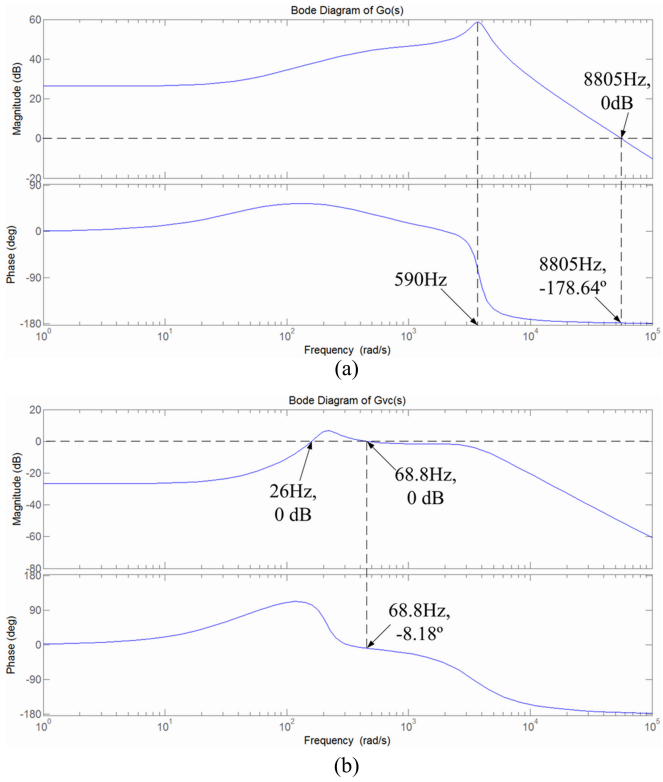

Fig. 5. Bode diagrams of the transfer functions from reference to output. (a) Without controllers. (b) With controllers.

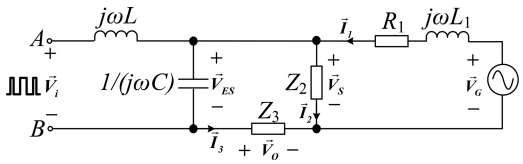

Fig. 6. Simplified vector circuit of Fig. 1(a).

III. Analysis of the ES With δ Control

Steady-state analysis using vector diagrams for δ control in four critical compensations is focused based on the simplified vector circuit where the inverter is replaced by its output voltage $\vec{V}_i$, as shown in Fig. 6.

A. δ Control Algorithm in Pure Reactive Power Compensation of the ES

1) Critical Load is Resistive: In Fig. 6, the input voltage is

$$\vec{V}_G = \vec{V}_S + \vec{I}_1(R_1 + j\omega L_1) = \vec{V}_S + (\vec{I}_2 + \vec{I}_3)(R_1 + j\omega L_1) = \vec{V}_{G1} + \vec{I}_3(R_1 + j\omega L_1) \tag{16}$$

where

$$\vec{V}_{G1} = \frac{R_1 + R_2 + j\omega L_1}{R_2} \times \vec{V}_S. \tag{17}$$

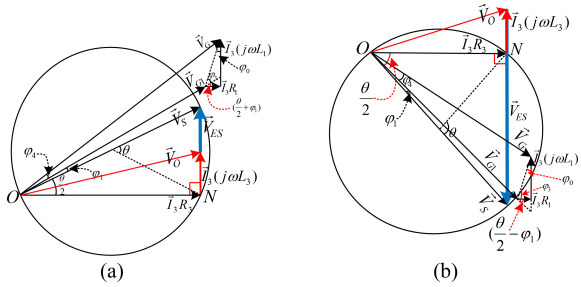

Fig. 7. Vector diagrams with resistive critical load and for pure reactive power compensation of the ES. (a) Inductive mode. (b) Capacitive mode.

The amplitude and phase angle of vector $\vec{V}_{G1}$ are

$$V_{G1} = \frac{\sqrt{(R_1 + R_2)^2 + (\omega L_1)^2}}{R_2} \times V_S \tag{18}$$

$$\varphi_1 = \tan^{-1}\left(\frac{\omega L_1}{R_1 + R_2}\right). \tag{19}$$

According to the Kirchhoff's voltage law (KVL), the relationship between $\vec{V}_{\rm ES}$ and $\vec{V}_O$ is

$$\vec{V}_S = \vec{V}_{\rm ES} + \vec{V}_O. \tag{20}$$

Pure reactive power compensation means the phase angle between $\vec{V}_{\rm ES}$ and $\vec{I}_3$ always keeps 90°, either leading or lagging. Thus, a circle can be depicted as shown in Fig. 7. The traces of point N in both figures are along the circles. Inductive mode is defined as $\vec{V}_{\rm ES}$ leading $\vec{I}_3$ by 90° and capacitive mode is defined as lagging. Resistive mode is the case when the ES voltage is nearly zero.

In Fig. 7(a) where the ES operates in inductive mode, geometric relationships can be obtained as

$$V_{\rm ES} = V_S \sin\left(\frac{\theta}{2}\right) - I_3 X_3 \tag{21}$$

where X_3 is positive at inductive mode, zero at resistive mode and negative at capacitive mode, respectively

$$I_3 = \frac{V_S}{R_3}\cos\left(\frac{\theta}{2}\right) \tag{22}$$

$$\varphi_0 = \tan^{-1}\left(\frac{R_1}{\omega L_1}\right) \tag{23}$$

$$\varphi_3 = \frac{\pi}{2} - \varphi_0 - \left(\frac{\theta}{2} + \varphi_1\right). \tag{24}$$

The law of cosines can be expressed in Fig. 7(a) as

$$\cos(\pi - \varphi_3) = \frac{I_3^2[R_1^2 + (\omega L_1)^2] + V_{G1}^2 - V_G^2}{2V_{G1}I_3\sqrt{R_1^2 + (\omega L_1)^2}}. \tag{25}$$

Substituting (22) into (25) yields

$$\sin\left(\theta + \tan^{-1}\left(\frac{b}{a}\right)\right) = m \tag{26}$$

where

$$\begin{cases} a = \frac{V_{G1}V_S}{R_3}\sqrt{R_1^2+(\omega L_1)^2}\cos(\varphi_0+\varphi_1) \\ b = \frac{V_S^2[R_1^2+(\omega L_1)^2]}{2R_3^2} + \frac{V_{G1}V_S}{R_3}\sqrt{R_1^2+(\omega L_1)^2}\sin(\varphi_0+\varphi_1) \\ m = \frac{V_G^2-V_{G1}^2-b}{\sqrt{a^2+b^2}}, m \in [-1,\ 1]. \end{cases} \tag{27}$$

The value of θ is determined by the operating function of the noncritical load and limited by (22). Then, solving (26) for θ yields

$$\theta = \sin^{-1}(m) - \tan^{-1}\left(\frac{b}{a}\right). \tag{28}$$

The law of sines can be expressed in Fig. 7(a) as

$$\frac{I_3\sqrt{R_1^2+(\omega L_1)^2}}{\sin(\varphi_4)} = \frac{V_G}{\sin(\pi-\varphi_3)}. \tag{29}$$

Substituting (22) and (24) into (29) gives

$$\sin(\varphi_4) = \frac{V_S\sqrt{R_1^2+(\omega L_1)^2}}{R_3V_G}\cos\left(\frac{\theta}{2}\right) \times \cos\left(\frac{\theta}{2}+\varphi_0+\varphi_1\right). \tag{30}$$

Since the voltage on the line impedance is smaller compared to V_G and V_{G1}, φ_4 should be an acute angle. Hence, the solution of (30) is expressed as

$$\varphi_4 = \sin^{-1}\left(\frac{V_S\sqrt{R_1^2+(\omega L_1)^2}}{R_3V_G}\cos\left(\frac{\theta}{2}\right) \times \cos\left(\frac{\theta}{2}+\varphi_0+\varphi_1\right)\right). \tag{31}$$

δ is defined as the phase angle that $\vec{V}_S$ lags $\vec{V}_G$, which can be expressed as

$$\delta = \varphi_1 + \varphi_4. \tag{32}$$

Formulas for δ calculation in Fig. 7(b) are the same as those in Fig. 7(a), and the only difference is that the value of θ is positive in the inductive mode, negative in the capacitive mode and zero in the resistive mode.

With δ control, some limitations and operating ranges of the ES can be revealed. Since noncritical load voltage can be obtained through I_3 multiplied by Z_3, it is found from (22) that the value of V_O decreases as θ increases. An extreme case is that θ is near π, which means $V_{\rm ES}$ is extremely big while V_O is nearly zero. It is unacceptable because there is almost no voltage on the noncritical load that it cannot take the role of a load.

The value of θ is related to circuit parameters and line voltage, which offers one rule for parameter selection. Another constraint is related to *m* in (27) which gives operating ranges of the ES, the upper and lower limits occur when *m* equals to 1 and –1, respectively. In other words, if the operating range is defined, (26) gives the limitations for selecting circuit parameters and examples are shown in Table II.

TABLE II
EFFECTIVE OPERATING VOLTAGE RANGES VERSUS PARAMETERS OF THE ES

Length of transmission line	Critical load: (Ω)	Noncritical load: (Ω)	Calculated effective operating range: (V)
2 km ($\boldsymbol{R_1 = 0.1\ \Omega}$ $\boldsymbol{L_1 = 2.4}$ **mH)**	53	57.5	220–222
	53	30	219–223
	53	10	214–230
	53	3	199–254
	43.5	**2.2**	**192–267**
200 m	**43.5**	**2.2**	**216–225**
500 m	**43.5**	**2.2**	**213–231**
1 km	**43.5**	**2.2**	**205–242**
4 km	**43.5**	**2.2**	**170–321**

In a distributed renewable power system, line impedances are related to distances [15]. It is seen from Table II that the operating ranges of the ESs decreases as the value of noncritical load increases. And also the longer the distance is, the larger operating range is, which offers a rule for the distribution of the ESs. For instance, the calculated operating range is 216 to 225 V with the transmission line for 200 m, which is within the tolerances of most critical loads and there is no need to locate the ES within such distance. Based on existing critical and noncritical loads at a single location, the operating ranges need to be checked before allocating and activating any ESs. If an ES has already been located where the calculated operating voltage range is too small, possible solutions are to reallocate the critical and noncritical loads in a proper proportion or relocate the ES.

2) Critical Load is Inductive: In Fig. 6, if Z_2 is inductive, the input voltage is

$$\begin{aligned} \vec{V}_G &= \vec{V}_S + \vec{I}_1(R_1+j\omega L_1) \\ &= \vec{V}_S + \left(\frac{\vec{V}_S}{R_2+j\omega L_2} + \vec{I}_3\right)(R_1+j\omega L_1) \\ &= \vec{V}_{G1} + \vec{I}_3(R_1+j\omega L_1) \end{aligned} \tag{33}$$

where

$$\vec{V}_{G1} = \frac{R_1+R_2+j\omega(L_1+L_2)}{R_2+j\omega L_2}\vec{V}_S \tag{34}$$

$$V_{G1} = V_S\sqrt{\frac{(R_1+R_2)^2+[\omega(L_1+L_2)]^2}{R_2^2+(\omega L_2)^2}} \tag{35}$$

$$\phi_1 = \tan^{-1}\left[\frac{\omega(L_1+L_2)}{R_1+R_2}\right] - \tan^{-1}\left(\frac{\omega L_2}{R_2}\right). \tag{36}$$

According to (20), the right-angled triangle including $\vec{I}_3R_3$, $(j\vec{I}_3X_3+\vec{V}_{\rm ES})$ and $\vec{V}_S$ in Fig. 7 will not change whatever the characteristics the critical load are. And geometrical relationships of the vectors are also the same. Thus, the formulas for δ calculation are the same as described in part 1) while the values of V_{G1} and φ_1 are changed according to (35) and (36).

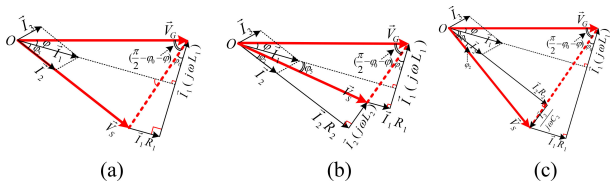

Fig. 8. Vector diagrams for the other three typical compensations of the ES. (a) Z_2 is resistive. (b) Z_2 is inductive. (c) Z_2 is capacitive.

3) Critical Load is Capacitive: This part is similar with part 2). In Fig. 6, if Z_2 is capacitive, the input voltage is

$$\begin{aligned}\vec{V}_G &= \vec{V}_S + \vec{I}_1(R_1 + j\omega L_1) \\ &= \vec{V}_S + \left(\frac{\vec{V}_S}{R_2 + \frac{1}{j\omega C_2}} + \vec{I}_3\right)(R_1 + j\omega L_1) \\ &= \vec{V}_{G1} + \vec{I}_3(R_1 + j\omega L_1) \qquad (37)\end{aligned}$$

$$\vec{V}_{G1} = \frac{1 - \omega^2 L_1 C_2 + j\omega C_2(R_1 + R_2)}{1 + j\omega R_2 C_2}\vec{V}_S \qquad (38)$$

$$V_{G1} = V_S\sqrt{\frac{(1 - \omega^2 L_1 C_2)^2 + [\omega C_2(R_1 + R_2)]^2}{1 + (\omega R_2 C_2)^2}} \qquad (39)$$

$$\varphi_1 = \tan^{-1}\left[\frac{\omega C_2(R_1 + R_2)}{1 - \omega^2 L_1 C_2}\right] - \tan^{-1}(\omega R_2 C_2). \qquad (40)$$

Vector diagrams are the same as shown in Fig. 7. The formulas for δ calculation are the same as part 1), except for $\vec{V}_{G1}$. One remark is that the operating ranges change as the critical loads vary because $\vec{V}_{G1}$ is changed and values in (27) will be changed. If the real part of noncritical load is not changed and all the other parameters are kept the same, the operating range will also be the same, whatever the noncritical loads are resistive, inductive or capacitive.

B. δ Control Algorithm in Specified PF Control of the ES

The ESs also has the potential to adjust PF of the input voltage sources. According to types of the critical and noncritical loads, nine situations should be presented. However, it is found that noncritical loads do not affect the triangle in bold lines in Fig. 8, which includes $\vec{V}_G$ and $\vec{V}_S$, where φ is defined as the phase angle that $\vec{I}_1$ lags $\vec{V}_G$, φ_2 is the impedance angle of the critical load, φ_5 is defined as the phase angle that $\vec{I}_1$ leads $\vec{V}_S$. Phase angles are also marked in Fig. 8.

In the triangle in bold, the law of sines is expressed as

$$\frac{V_S}{\sin\left(\frac{\pi}{2} - \varphi_0 - \varphi\right)} = \frac{V_G}{\sin\left[\pi - \varphi_5 - \left(\frac{\pi}{2} - \varphi_0\right)\right]} \qquad (41)$$

$$\delta = \varphi + \varphi_5. \qquad (42)$$

φ_5 can be calculated through (41) if φ is given and δ can be calculated for the specified PF control. It is also found that the algorithms are the same whatever the critical loads are inductive, resistive or capacitive. The remark is that the effective operating range is limited by (41). By substituting parameters in Table I into (23) and (41), it is found that the effective operating voltage range of specified PF control decreases as PF increases.

C. δ Control Algorithm in Constant Real Power Compensation of the ES

The ESs can also support constant real power compensation, which can also been described by Fig. 8. Complex powers of $\vec{V}_G$ and $\vec{I}_1$ are

$$\begin{aligned}\tilde{S} &= \vec{V}_G \cdot \vec{I}_1^* = V_G \angle 0^\circ \cdot I_1 \angle \varphi \\ &= V_G I_1(\cos\varphi + j\sin\varphi) = P + jQ \qquad (43)\end{aligned}$$

where

$$P = V_G I_1 \cos\varphi \qquad (44)$$

$$Q = V_G I_1 \sin\varphi. \qquad (45)$$

Once V_G is given, constant P means $I_1\cos\varphi$ keeps constant. The law of sines in the triangle is

$$\begin{aligned}\frac{V_S}{\sin\left(\frac{\pi}{2} - \varphi_0 - \varphi\right)} &= \frac{V_G}{\sin\left[\pi - \varphi_5 - \left(\frac{\pi}{2} - \varphi_0\right)\right]} \\ &= \frac{I_1\sqrt{R_1^2 + (\omega L_1)^2}}{\sin\delta}. \qquad (46)\end{aligned}$$

Obviously, if P is given, unknown parameters such as δ and φ can be determined and solved by (41), (42), (44) and (46). It is found that only one parameter of P, δ or φ can be given and the other two will be determined by the known one. For instance, if P is given manually, the values of δ, φ, and PF will be determined accordingly.

D. δ Control Algorithm in Constant Reactive Power Compensation of the ES

The ESs can also support constant reactive power compensation which is similar with constant real power compensation. δ can be calculated by solving (41), (42), (45) and (46). Once Q is given, all the other parameters can also be determined.

IV. Simulations and Discussions

To verify the aforementioned analysis, simulations are conducted based on parameters shown in Table I. The control objectives are: 1) Critical load voltage is regulated to 220 V. 2) For pure reactive power compensation, the phase angle between ES voltage and current should be 90°. For specified PF control, PF should be the same as defined. For constant real power compensations, the related powers should be the same as defined.

A. Pure Reactive Power Compensation of the ES

1) Both Critical Load and Noncritical Load are Resistive: Fig. 9 shows the simulated waveforms of the ES for pure reactive power compensation. It can be seen that the voltages of critical loads are regulated to 220 V with different V_G. At 0.583 s in Fig. 9(c), the noncritical load voltage reaches its maximum value while the ES voltage is zero, which means the ES current leads the ES voltage by 90° and the ES operates in capacitive mode. However, in Fig. 9(b), one zero crossing

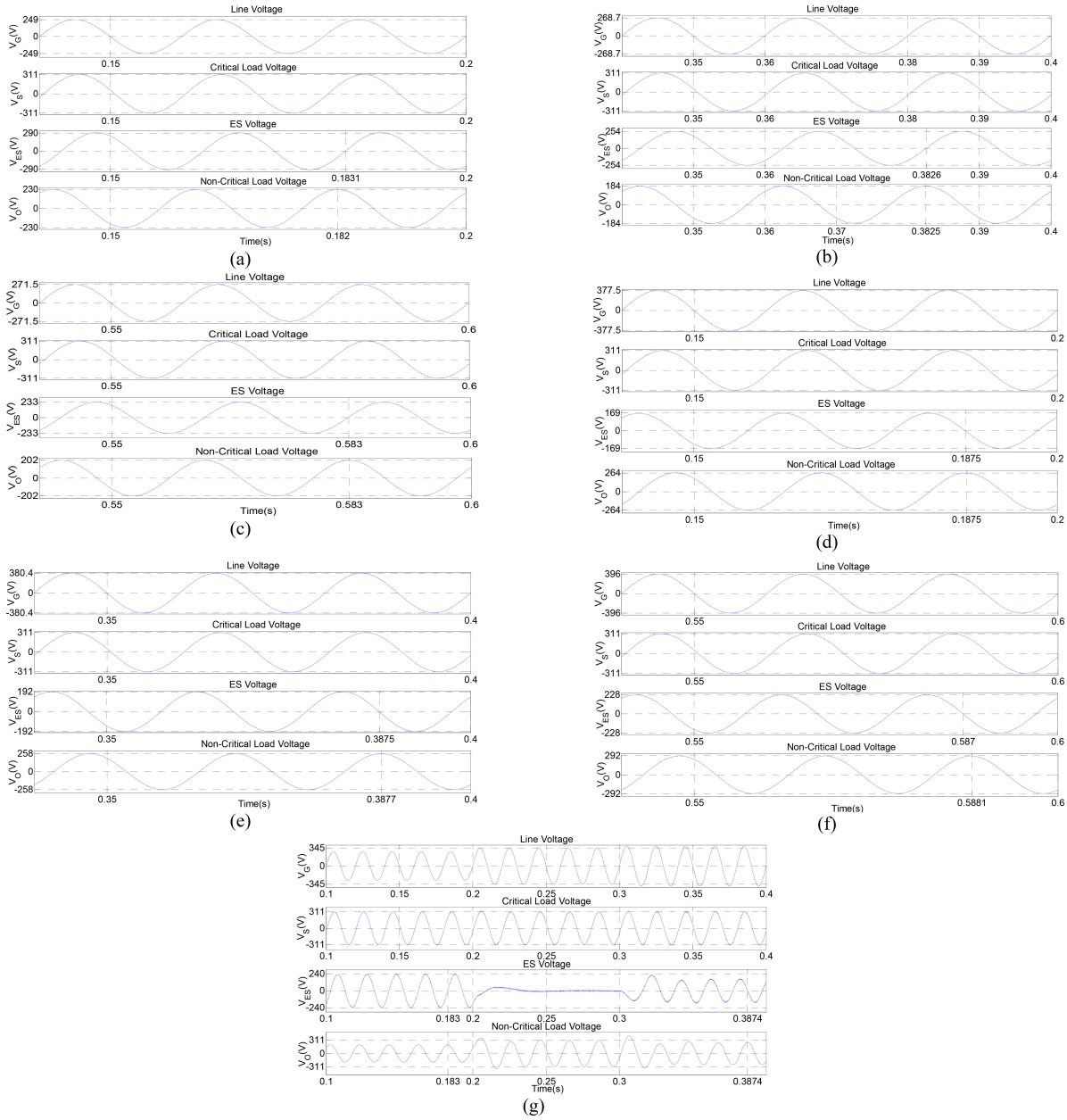

Fig. 9. Simulation waveforms @ $Z_2 = 43.5\ \Omega$ and $Z_3 = 2.2\ \Omega$ for pure reactive power compensations of the ES. Ch1 to Ch4: line voltage, critical load voltage, ES voltage and noncritical load voltage. (a) $V_G = 176$ V. (b) $V_G = 190$ V. (c) $V_G = 192$ V. (d) $V_G = 267$ V. (e) $V_G = 269$ V. (f) $V_G = 280$ V. (g) Transient response while V_G varies from 198 to 244 V and then to 256 V.

point of the ES voltage is at 0.3826 s while the time when the noncritical load voltage reaches peak value is at 0.3825 s. The severer case happens in Fig. 9(a) where the times are 0.1831 and 0.182 s, respectively. Fig. 9(a) and (b) shows that the phase angle between the ES current and voltage is between 90° and 180°, which means the ES is not in pure reactive power compensation but in capacitive plus negative real power compensation instead. The same analogy applies to Fig. 9(d)–(f). The ES operates in inductive mode in Fig. 9(d) but in inductive plus negative real power compensation in Fig. 9(e) and (f). The effective operating voltage range can be easily obtained from Fig. 9 to be 192 to 267 V between which the ES operates in reactive power compensation. It is preferred that the ES operates within the effective range because the mean current through the dc side will be zero and less discharge or charge times will enhance the reliability of the batteries. In order to check the performance of the controllers, transient responses are presented in Fig. 9(g). V_G is 198 V between 0.1 and 0.2 s, during which the ES operates in capacitive mode. At the moment of 0.2 s, V_G rises from 198 to 244 V suddenly and the ES changes to resistive mode in about two to three cycles and last till 0.3 s. Another sudden change happens at 0.3 s when V_G rises to 256 V, under which the ES operates in inductive mode. It is observed that it takes about two to three cycles to get steady and also the critical load

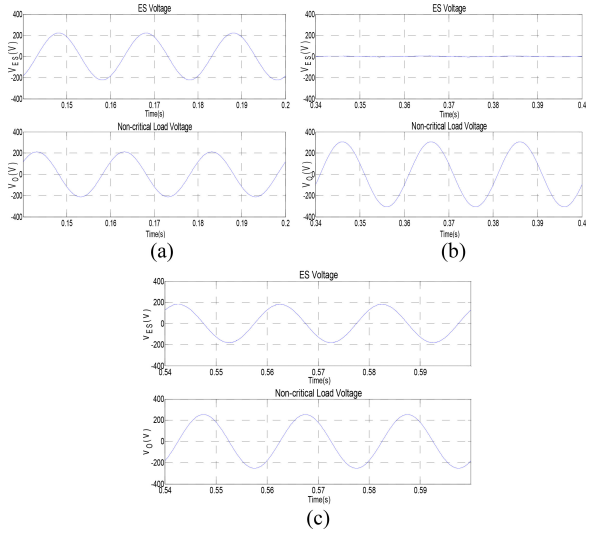

Fig. 10. Simulation waveforms of $Z_2 = 43.5 + j18.85\ \Omega$ and $Z_3 = 2.2\ \Omega$ for pure reactive power compensation of the ES. (a) $V_{\rm ES}$ and V_O @ $V_G = 193$ V. (b) $V_{\rm ES}$ and V_O @ $V_G = 244.7$ V. (c) $V_{\rm ES}$ and V_O @ $V_G = 269$ V.

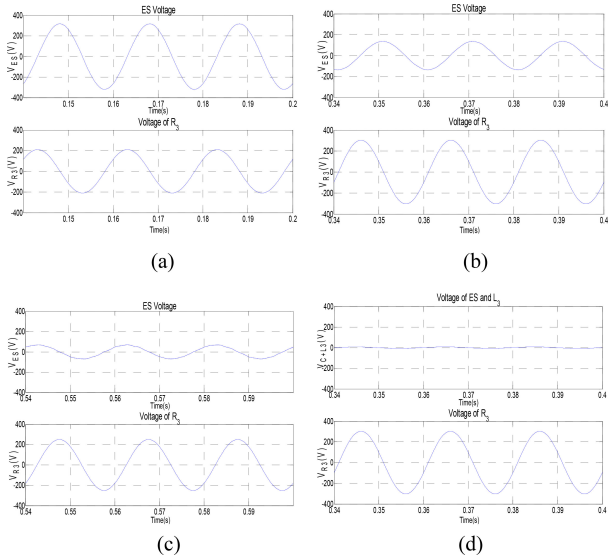

Fig. 11. Simulation waveforms of $Z_2 = 43.5 + j18.85\ \Omega$ and $Z_3 = 2.2 + j1\ \Omega$ for pure reactive power compensation of the ES. (a) $V_{\rm ES}$ and V_{R3} @ $V_G = 193$ V. (b) $V_{\rm ES}$ and V_{R3} @ $V_G = 244.7$ V. (c) $V_{\rm ES}$ and V_{R3} @ $V_G = 269$ V. (d) $V_{{\rm ES}+L3}$ and V_O @ $V_G = 244.7$ V.

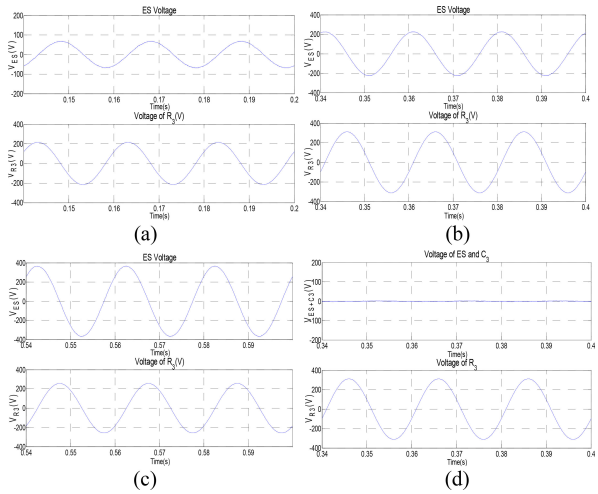

Fig. 12. Simulation waveforms of $Z_2 = 43.5 + j18.85\ \Omega$ and $Z_3 = 2.2 - j1.592\ \Omega$ for pure reactive power compensation of the ES. (a) $V_{\rm ES}$ and V_{R3} @ $V_G = 193$ V. (b) $V_{\rm ES}$ and V_{R3} @ $V_G = 244.7$ V. (c) $V_{\rm ES}$ and V_{R3} @ $V_G = 269$ V. (d) $V_{{\rm ES}+C3}$ and V_{R3} @ $V_G = 244.7$ V.

voltage almost keeps 220 V when V_G varies. Although there are transient voltage spikes seen on noncritical load, they are within the operating range and acceptable.

2) Critical Load is Inductive and Noncritical Load is Resistive: Fig. 10 shows the simulated results under the inductive critical load of $43.5 + j18.85\ \Omega$ and resistive noncritical load.

It is seen from Fig. 10 that the ES operates in three different kinds of modes as V_G varies. Although the results look similar as presented in part 1), the values of V_{G1} and φ_1 are different in the algorithm. The reactive power of the critical loads is compensated by the grid and has little influence on the operating mode of the ES. However, the existence of L_2 affects the PF of the ac source. δ control at such situation has been verified by the simulation results.

3) Critical Load is Inductive and Noncritical Load is Inductive: Another case in which both critical and noncritical loads are inductive is also simulated as shown in Fig. 11. Fig. 11(a) and (c) looks similar with Fig. 10. However, great difference has been seen when V_G is 244.7 V, under which the ES operates in resistive mode in Fig. 10(b), while still in capacitive mode in Fig. 11(b). The reason is that there is inductive reactive power due to the inductive part of Z_3, which needs to be compensated by the ES in addition. Thus, the ES has to operate in capacitive mode. If the ES capacitor and L_2 are regarded as one part together, the total voltage on both components will be zero, as seen in Fig. 11(d).

4) Critical Load is Inductive and Noncritical Load is Capacitive: Fig. 12 shows the results of the case when critical load is inductive and noncritical load is capacitive, which is similar with part 3). The difference is that the ES has to generate inductive reactive power to compensate the capacitive reactive power introduced by C_3.

B. Other Compensation Functions of the ES

Dc voltage is set to 720 V while the other parameters are the same as in Table I. The simulated results are shown in Fig. 13.

It can be seen from Fig. 13(a) that the line current is in phase with the voltage, which means unity PF is realized by δ control. Unity PF can also be proved by the result of reactive power, which is nearly 0 in Fig. 13 (b).

There are several groups of roots by solving equations for constant real power compensation. Considering some limitations such as no complex results, I_1 not negative, φ less than $\pi/2$ and δ not zero, there is only one adequate root left. If the real power is defined as 10 kW as an example, the calculated δ is 0.1447 when line voltage is 230 V. Then, the calculated RMS value of line current and φ are 44.74 A and 0.238 rad, respectively. It is shown in Fig. 13(b) that simulated P is 9.92 kW and the error is 0.8%, which is acceptable and validates the algorithm.

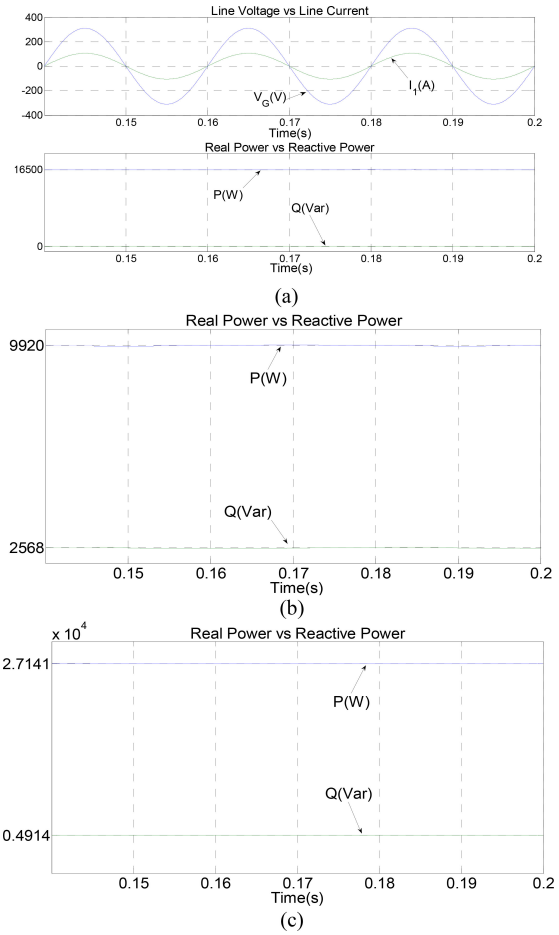

Fig. 13. Simulation waveforms @ $Z_2 = 43.5\ \Omega$, $Z_3 = 2.2\ \Omega$ for other three compensations of the ES. (a) Unity PF control @ $V_G = 220$ V. (b) Constant real power compensation @ $V_G = 230$ V. (c) Constant reactive power compensation @ $V_G = 230$ V.

Similarly, if the reactive power is defined as 5 kvar, the calculated δ is 0.4113 when line voltage is 230 V. The RMS values of line current and φ are 121.5 A and 0.18 rad, respectively, by setting which into the simulation, the simulated Q in Fig. 13(c) is 4.914 kvar and the error is 1.72%, which also validates the algorithm.

V. Experiments

To double check the effectiveness of the control strategy and analysis on the effective operating ranges of the ESs, an experimental study has been conducted. As mentioned, there are many situations if all kinds of critical and noncritical loads are considered. For concision of the paper, only the pure reactive power compensation, the most critical function of the ES, is presented as an example. If all the parameters for experiment are the same as simulation, the line current will be too large to be safely implemented in the lab. Moreover, bidirectional dc source or 40 batteries (12 V each) in series are needed as dc input for the inverter, which is also not available in the lab. Hence, a scale-down system is used in experiments. Six units of battery are used in series and V_S is set to 22 V. The parameters for the experiment are listed in Table III. One remark is that a switch is used to activate or deactivate the ES, as shown in Fig. 1(a). Parameters of the controllers are also list in Table III.

TABLE III
Experimental Setup of the ES

Regulated mains voltage (V_S)	22 V
Battery voltage (V_{dc})	72 V
Line resistance (R_1)	4 Ω
Line inductance (L_1)	84.1 mH
Critical load (R_2)	2000 Ω
Noncritical load (R_3)	101.4 Ω
Inductance of low-pass filter (L)	3 mH
Capacitance of low-pass filter (C)	50 μF
Switching frequency (f_s)	5 kHz
Calculated effective operating range of the ES	19.9–25.7 V
Software platform	DSP28335
Feedback coefficient of voltage loop (k_{vf})	0.5
Feedback coefficient of voltage loop (k_{if})	1
$V_{S_{kp}}$	0.1
$V_{S_{kr}}$	7
$I_{L_{kp}}$	0.1

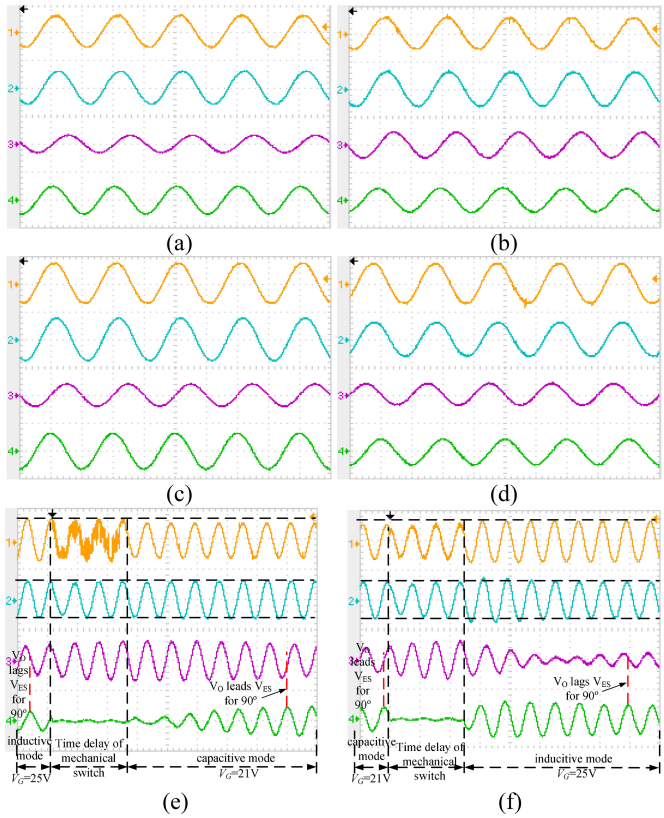

Fig. 14. Measured voltage waveforms @ the ES is within the effective operating range (50 V/div, 10 ms/div). Ch1: line voltage, Ch2: critical load voltage, Ch3: ES voltage, Ch4: noncritical load voltage. (a) ES is not activated @ $V_G = 20.2$ V. (b) ES is activated @ $V_G = 20.2$ V. (c) ES is not activated @ $V_G = 25.7$V. (d) ES is activated @ $V_G = 25.7$ V. (e) Transient response from inductive mode to capacitive mode. (f) Transient response from capacitive mode to inductive mode.

Fig. 14 shows the measured voltage waveforms under different conditions. It can be seen from Fig. 14(a) and (b) that the voltage on critical load is 20.9 and 21.9 V before and after the ES is activated when input voltage is 20.2 V. The critical load

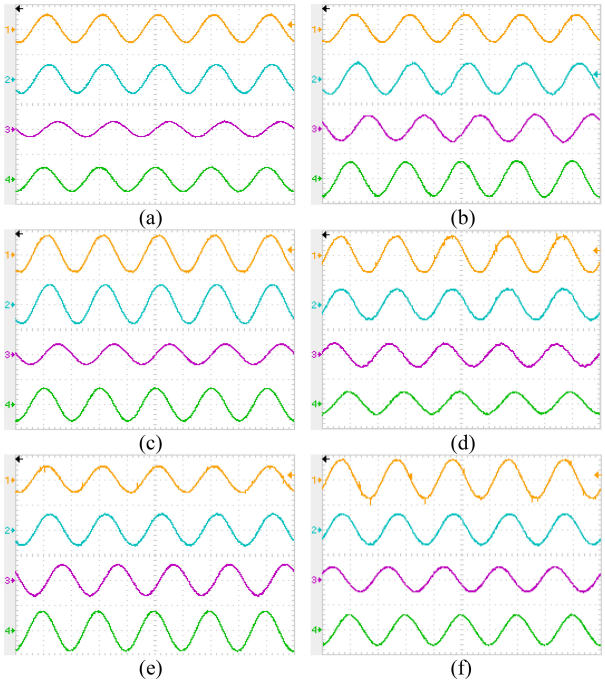

Fig. 15. Measured voltage waveforms @ the ES is out of the effective operating range (50 V/div, 10 ms/div). Ch1: line voltage, Ch2: critical load voltage, Ch3: ES voltage, Ch4: noncritical load voltage. (a) ES is not activated @ $V_G = 19.6$ V. (b) ES is activated @ $V_G = 19.6$ V. (c) ES is not activated @ $V_G = 26.1$ V. (d) ES is activated @ $V_G = 26.1$ V. (e) ES is activated @ $V_G = 18.4$ V. (f) ES is activated @ $V_G = 27.5$ V.

voltage is also regulated to about 22 V when V_G is 25.7 V in Fig. 14(d). The ES current which is in phase with noncritical load voltage always leads the ES voltage by 90° when the switch is off, as shown in Fig. 14(a) and (c). However, when the ES is activated in Fig. 14(b) and (d), it operates in capacitive mode at 20.2 V and in inductive mode at 25.7 V, respectively, which means the ES can operate in reactive power compensation mode within its effective operating voltage ranges. Transient responses of the ES are presented in Fig. 14(e) and (f). Since there is no programmable ac source in the lab, a monopole double throw switch is used to connect different variacs, of which one is set to 21 V and the other is set to 25 V. In the first period of Fig. 14(e), V_G is set to 25 V and the ES operates in inductive mode. Since the switch is operated manually, there is time delay from one variac to another during which the input voltage varies randomly. Thus, the waveforms during the delay time may be ignored. V_G is connected to 21 V after the delay time and the ES changes to capacitive mode. The transient responses in Fig. 14(f) are opposite with that in Fig. 14(e). V_G is connected to 21 V and the ES operates in capacitive mode during the first period. After the delay of mechanical switch by hand, V_G is connected to 25 V and the ES starts the inductive mode.

Fig. 15 shows the results when input voltages are out of the effective operating ranges for pure reactive power compensations where the critical load voltages are all regulated to 22 V with the ES being activated. 19.6 and 26.1 V are chosen to compare with the lower and upper limits considering tolerances. The ES operates in capacitive mode before being activated, as shown in Fig. 15(a) and (c). However, it is seen from Fig. 15(b) that the ES current leads its voltage by more than 90°, which means the ES does not operate in pure capacitive mode but in capacitive plus negative real power compensation, instead. Fig. 15(d) shows that the ES current lags its voltage by more than 90°, which means the ES does not operate in pure inductive mode but in the mode of inductive plus negative real power compensation. Thus, the battery will be discharged at both modes in Fig. 15(b) and (d) when the ES is operated out of the effective operating range. More obvious cases can be seen in Fig. 15(e) and (f) where the ES current and voltage are not perpendicular with each other. The batteries will be discharged, which is risky for normal operations of the ES. It is also noticed from Fig. 15(b) and (e) that the noncritical load voltage increases as line voltage decreases. Thus, the safety ranges of the ESs are related to the safety ranges of the noncritical loads.

VI. Conclusion

A novel control strategy, called δ control, has been proposed for the ESs and the steady-state analysis with different types of critical loads such as resistive, capacitive and inductive has been presented. By controlling a single parameter δ which contains all the control information for the reference of a PR controller, the critical load voltage is regulated to the predefined reference and different power compensation functions of the ESs can be achieved. Four critical compensations, namely, pure reactive power compensation, specified PF compensation, constant real power compensation and constant reactive power compensation, have been considered, for which the essence is different phase relationships between ES voltage and current. Vector diagrams for different situations are depicted and algorithms at steady-state are derived for δ calculations. With δ control, the operating modes of the ESs can be automatically determined with different line voltages, and the same algorithms can be used for all the compensations when the reactive parts in noncritical loads change and the real parts keep the same. The ESs can operate in capacitive, resistive and inductive modes whatever characteristics the critical and noncritical loads are. Based on the geometrical relationships derived from the vector diagrams, the specific limitations and constraints of the ESs such as effective operating ranges and safety ranges have been revealed, offering guidelines on how to distribute the ESs in the distributed power systems effectively and economically. Both simulation and experiments have been conducted and the results validate the analysis of δ control, especially the effective operating ranges and safety ranges of the ESs.

References

[1] M. Cheng and Y. Zhu, "The state of the art of wind energy conversion systems and technologies: A review," *Energy Convers. Manag.*, vol. 88, pp. 332–347, Dec. 2014.

[2] K. Strunz, E. Abbasi, and D. N. Huu, "DC microgrid for wind and solar power integration," *IEEE J. Emerg. Sel. Topics Power Electron.*, vol. 2, no. 1, pp. 115–126, Mar. 2014.

[3] J. Han, S. K. Solanki, and J. Solanki, "Coordinated predictive control of a wind/battery microgrid system," *IEEE J. Emerg. Sel. Topics Power Electron.*, vol. 1, no. 4, pp. 296–305, Dec. 2013.

[4] C. O. Gercek and M. Ermis, "Elimination of coupling transformer core saturation in cascaded multilevel converter-based T-STATCOM systems," *IEEE Trans. Power Electron.*, vol. 29, no. 12, pp. 6796–6809, Dec. 2014.

[5] P. Sotoodeh and R. D. Miller, "Design and implementation of an 11-level inverter with FACTS capability for distributed energy systems," *IEEE J. Emerg. Sel. Topics Power Electron.*, vol. 2, no. 1, pp. 87–96, Mar. 2014.
[6] T. J. Dionise, "Assessing the performance of a static var compensator for an electric arc furnace," *IEEE Trans. Ind. Appl.*, vol. 50, no. 3, pp. 1619–1629, May/Jun. 2014.
[7] S. X. Du, J. J. Liu, J. L. Lin, and Y. J. He, "A novel DC voltage control method for STATCOM based on hybrid multilevel H-Bridge converter," *IEEE Trans. Power Electron.*, vol. 28, no. 1, pp. 101–111, Jan. 2013.
[8] B. Gultekin and M. Ermis, "Cascaded multilevel converter-based transmission STATCOM: System design methodology and development of a 12 kV $\pm$12 MVAr power stage," *IEEE Trans. Power Electron.*, vol. 28, no. 11, pp. 4930–4950, Nov. 2013.
[9] C. Wang, X. Yin, Z. Zhang, and M. Wen, "A novel compensation technology of static synchronous compensator integrated with distribution transformer," *IEEE Trans. Power Del.*, vol. 28, no. 2, pp. 1032–1039, Apr. 2013.
[10] Z. Song and V. Vittal, "Design of wide-area power system damping controllers resilient to communication failures," *IEEE Trans. Power Syst.*, vol. 28, no. 4, pp. 4292–4300, Nov. 2013.
[11] B. Kazemtabrizi and E. Acha, "An advanced STATCOM models for optimal power flows using Newton's method," *IEEE Trans. Power Syst.*, vol. 29, no. 2, pp. 514–525, Mar. 2014.
[12] S. Y. R. Hui, C. K. Lee, and F. Wu, "Electric springs—A new smart grid technology," *IEEE Trans. Smart Grid*, vol. 3, no. 3, pp. 1552–1561, Sep. 2012.
[13] S. C. Tan, C. K. Lee, and S. Y. R. Hui, "General steady-state analysis and control principle of electric springs with active and reactive power compensations," *IEEE Trans. Power Electron.*, vol. 28, no. 8, pp. 3958–3969, Aug. 2013.
[14] P. Kanjiya and V. Khadkikar, "Enhancing power quality and stability of future smart grid with intermittent renewable energy sources using electric springs," in *Proc. Int. Conf. Renewable Energy Res. Appl.*, 2013, pp. 918–922.
[15] C. K. Lee, B. Chaudhuri, and S. Y. R. Hui, "Hardware and control implementation of electric springs for stabilizing future smart grid with intermittent renewable energy sources," *IEEE J. Emerging Sel. Topics Power Electron.*, vol. 1, no. 1, pp. 18–27, Mar. 2013.
[16] S. Yan, S. C. Tan, C. K. Lee, and S. Y. R. Hui, "Electric spring for power quality improvement," in *Proc. 29th IEEE Appl. Power Electron. Conf. Expo.*, 2014, pp. 2140–2147.
[17] N. R. Chaudhuri, C. K. Lee, B. Chaudhuri, and S. Y. R. Hui, "Dynamic modeling of electric springs," *IEEE Trans. Smart Grid*, vol. 5, no. 5, pp. 2450–2458, Sep. 2014.

Qingsong Wang (S'14) received the B.Sc. and M.Sc. degrees in electrical engineering from Zhejiang University, Hangzhou, China, in 2004 and 2007, respectively. He is currently working toward the Ph.D. degree in electrical engineering at Southeast University, Nanjing, China.

From July 2004 to July 2005, he was an Engineer in Shihlin Electronic & Engineering Co., Suzhou, China. From July 2007 to August 2011, he was an Engineer in Global Development Center, Philips Lighting Electronics, Shanghai, China. In October 2010, he was promoted to be a Senior Engineer. From August 2011 to September 2013, he was a Lecturer in the PLA University of Science and Technology, Nanjing. His current research interests include electronic ballasts, multilevel rectifiers of current source, and applications of power electronics to power systems.

Ming Cheng (M'01–SM'02–F'15) received the B.Sc. and M.Sc. degrees from the Department of Electrical Engineering, Southeast University, Nanjing, China, in 1982 and 1987, respectively, and the Ph.D. degree from the Department of Electrical and Electronic Engineering, University of Hong Kong, Hong Kong, in 2001.

Since 1987, he has been with Southeast University, where he is currently a Distinguished Professor in the School of Electrical Engineering and the Director of the Research Center for Wind Power Generation. His teaching and research interests include electrical machines, motor drives for electric vehicles, and renewable energy generation. He has authored or coauthored more than 300 technical papers and four books and is the holder of 55 patents in these areas. He is a Distinguished Lecturer of the IEEE Industry Applications Society in 2015/2016.

Dr. Cheng is a Fellow of the Institution of Engineering and Technology. He has served as chair and organizing committee member for many international conferences.

Zhe Chen (M'95–SM'98) received the B.Eng. and M.Sc. degrees from the Northeast China Institute of Electric Power Engineering, Jilin City, China, and the Ph.D. degree from the University of Durham, Durham, U.K.

He is a Full Professor with the Department of Energy Technology, Aalborg University, Aalborg, Denmark. He is the Leader of Wind Power System Research Program, Department of Energy Technology, Aalborg University, and the Danish Principal Investigator for the Wind Energy of Sino-Danish Center for Education and Research. His research interests include power systems, power electronics and electric machines, and his main current research interests are wind energy and modern power systems. He has led many research projects and has more than 400 publications in his technical field. He is an Editor of the IEEE TRANSACTIONS ON POWER SYSTEMS, and an Associate Editor of the IEEE TRANSACTIONS ON POWER ELECTRONICS.

Dr. Chen is a Fellow of the Institution of Engineering and Technology (London, U.K.), and a Chartered Engineer in the U.K.

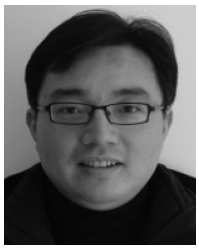

Zheng Wang (S'05–M'09–SM'14) received the B.Eng. and M.Eng. degrees from Southeast University, Nanjing, China, in 2000 and 2003, respectively, and the Ph.D. degree from the University of Hong Kong, Hong Kong, in 2008.

From 2008 to 2009, he was a Postdoctoral Fellow in Ryerson University, Toronto, ON, Canada. He is currently an Associate Professor in the School of Electrical Engineering, Southeast University. His research interests include electric drives, power electronics, and distributed generation. He has authored or coauthored more than 70 internationally refereed papers and four books in these areas.

Dr. Wang received several academic awards including IEEE PES Chapter Outstanding Engineer Award, Best Paper Award of International Conference on Electrical Machines and Systems, Best Session Paper Award of IEEE Annual Meeting of Industrial Electronics, and Nanjing Outstanding Paper Award of *Natural Science*.